*Journal of Applied Fluid Mechanics*, Vol. 17, No. 11, pp. 2499-2513, 2024.
Available online at www.jafmonline.net, ISSN 1735-3572, EISSN 1735-3645.
https://doi.org/10.47176/jafm.17.11.2467

# Investigation and Optimization of Wave Suppression Baffles in Automobile Integrated Water Tanks

F. Dong†, X. Xu, W. Zhang, W. Hu and X. Cao

*School of Automotive and Traffic Engineering, Jiangsu University, Zhenjiang 212013, China*

†*Corresponding Author Email: jsdxdf@ujs.edu.cn*

## ABSTRACT

The risk of liquid agitation in pump-driven tanks within integrated tanks has significantly escalated due to the growing demands for tank integration in new-energy vehicles. In order to solve the problem of liquid sloshing in integrated tanks, this paper presents the design of a baffle structure aimed at reducing waves in integrated water tanks. The numerical simulation method of combining the level-set function with the volume of fluid (CLSVOF) has been employed, significantly enhancing the accuracy of numerical calculations related to a two-phase flow field inside an integrated tank. A comparison was made by analyzing different factors, notably baffle length ($L$), baffle depth ($H$), and baffle angle ($\theta$), to investigate their influences in suppressing liquid agitation within the integrated water tank. Numerical computations were conducted utilizing design points acquired by the Latin hypercube sampling technique. The Kriging approximation modelling method was employed to hold down computing time. The Pareto solution was obtained by means of the non-dominated sorting genetic algorithm II, while the optimal solution set was evaluated and ranked using the multi-criteria decision-making algorithm (MCDM). The results show that increasing the baffle depth within a certain range can effectively suppress the wave height in the tank. When the baffle depth is increased to a certain value, the effect on wave-height suppression in the water tank is limited. When the baffle length and angle of the baffle exceed a certain value, it will also have the effect of suppressing the wave height in the tank. After comparing various factors of the baffle, it was ultimately found that the wave suppression effect is maximal when the length of the baffle is 13 millimeters, the depth of the baffle is 49 millimeters, and the angle of the baffle is -20 degrees. The main contribution of this study is the proposed wave-suppressing baffle structure, which provides new insights for the future structural design of integrated water tanks.

***Article History***

*Received November 28, 2023*
*Revised May 6, 2024*
*Accepted May 23, 2024*
*Available online September 1, 2024*

***Keywords:***

*Liquid sloshing*
*Wave suppression baffle*
*Automobile integrated water tank*
*Optimization*
*Kriging approximation modelling method*

## 1. INTRODUCTION

The goal of carbon neutrality has garnered widespread international agreement and is serving as a catalyst for the ongoing shift towards renewable energy sources. The objective of achieving carbon peaking and carbon neutrality has presented novel obstacles in the automotive sector. During the New Energy Vehicle Conference, it was emphasized that the adoption of electric propulsion is the primary approach towards achieving carbon reduction. The primary distinction between new energy vehicles and conventional vehicles is not just attributed to the incorporation of the key components known as the "three electric" but also to the integration of a much-enhanced thermal management system. The integration of water tanks has emerged as a prominent area of research within the realm of vehicle thermal management technologies. The incorporation of a valve island within the refrigerant circuit, together with the integration of several valves into the water tank itself, enhances the overall simplicity and organization of the vehicle, while concurrently leading to cost reduction. The coordination of the vehicle's independent battery cooling circuit, motor cooling circuit, and heating circuit is achieved by means of an integrated valve island, which ensures the maintenance of a steady temperature for these three electrical systems. The tank's complexity has experienced a notable escalation because of the significant enhancement in the tank's integration roles. The integrated tank is linked to three circuits that correspond to the water

**NOMENCLATURE**

| | | | |
|---|---|---|---|
| $L$ | baffle length | $H$ | baffle depth |
| $\theta$ | baffle angle | $\eta$ | wave height difference |
| $V_{air}$ | the volume of air | | |

pump. The pump propels the liquid within the tank, resulting in increased liquid fluctuations. Consequently, the liquid exerts a crushing effect on the tank walls. The presence of air in the liquid that has been disturbed by the pumping action results in the incorporation of air bubbles into both the pipeline and the pump. This phenomenon has a detrimental impact on the operation of the pump as well as on other associated equipment. Therefore, it is crucial to address liquid agitation within integrated tanks (Tian & Gu, 2019; Li et al., 2023).

Extensive theoretical and experimental research has been conducted on the sloshing of liquid within tanks. Many researchers have thoroughly investigated the problem of liquid sloshing, as well as the associated numerical simulation methods. Most numerical simulations have focused on grid-based methods. Wu et al. (1998) analyzed the sloshing waves in a three-dimensional cavity using a finite element method based on fully nonlinear potential theory. Chen and Nokes (2005) proposed a novel time-invariant finite difference method for analyzing the fully two-dimensional sloshing motion within a tank. Mitra et al. (2008) studied tank sloshing using a finite difference approach. Faltinsen et al. (2005) classified the steady-state three-dimensional (3D) resonant waves in a tank using an asymptotic modal system and analyzed the steady-state motions regarding the function domain frequency with respect to the mean fluid depth and forcing amplitude. Faltinsen and Timokha (2010) studied the forced sloshing of a two-dimensional liquid within a circular cavity using a multimode method. Liu and Lin (2008) performed numerical simulations of three-dimensional free-surface sloshing using the volume-of-fluid (VOF) method, considering six-degree-of-freedom excitations in non-inertial coordinates. The complexity and nonlinearity of liquid sloshing pose challenges to theoretical studies. Subsequently, research has begun to integrate numerical simulations with experiments, which has provided a deeper understanding of liquid sloshing within tanks. Maleki and Ziyaeifar (2008) conducted hydrodynamic damping experiments on the sloshing in a cylindrical tank by adding baffles of various shapes and found that ring-shaped baffles are effective in reducing sloshing oscillations. Shao et al. (2012) proposed an improved smoothed particle hydrodynamics (SPH) method for numerical calculations of viscous incompressible liquid sloshing, with simulation results including flow patterns, wave heights, pressure fields, and wall pressure loads that were consistent with experimental results. Zhang et al. (2023) compared experimental and numerical simulations of tank sloshing in regular waves constrained to two degrees of freedom (heave and pitch), investigating the multiphase flow field within the tank and achieved good agreement between experimental and simulated results.

The investigation of liquid sloshing revealed that baffles serve as a damping mechanism to successfully mitigate adverse liquid sloshing phenomena. Baffles are strategically incorporated inside the tank structure to enhance the dissipation of wave energy and minimize hydrodynamic loads. Ebrahimian et al. (2013) proposed the utilization of the boundary element approach to ascertain the frequency and mode of natural sloshing in axisymmetric vessels that have many baffles. The problem of liquid sloshing in a two-dimensional rectangular tank with baffles was addressed through the development of a viscous-fluid model that utilized a non-inertial reference system (Lu et al., 2015). Xue et al. (2017) examined the mitigation of sloshing pressure in tanks by employing various baffle structures. Their findings suggest that the use of vertical baffles can alter the flow dynamics and change the primary intrinsic frequency within tanks, successfully reducing the impact of shock pressure on the tank walls. It is important to highlight that the installation of many baffles in a tank is more effective than using a single baffle (Xue et al., 2017). Kolaei et al. (2015) developed a boundary element approach for the purpose of determining the natural frequencies and modes of oscillation in horizontally moving cylindrical vessels that are partially filled and equipped with longitudinal baffles of varying configurations. Chu et al. (2018) examined the impact of various configurations of baffle spacing and height on the phenomenon of liquid sloshing. To study this, they employed the technique of large eddy simulation (LES). The findings of their study revealed that the presence of multiple baffles results in a more effective reduction of hydrodynamic forces than the utilization of a single baffle (Chu et al., 2018). Ma et al. (2021) utilized the lattice Boltzmann method (LBM) to assess the effectiveness of single and double vertical baffles positioned at various heights and spacings. A study conducted by Jin et al. (2022) using an internal Navier-Stokes model, examined the impact of apertures and inclined baffles on the mitigation of liquid sloshing. Over the years, however, baffles have been only infrequently employed to limit fluid sloshing within automotive fuel tanks. Zhang (2020) investigated the impact of various baffle designs on both oil sloshing pressure and time-area values. He employed the VOF method to conduct this analysis. His team discovered that a corrugated bulkhead tank exhibits the least amount of sloshing pressure in the central location (Zhang et al., 2020). Following that, a comprehensive investigation was conducted on the impacts of six elements — specifically, baffle height, structure, form, spacing, number, and placement position — on the phenomenon of oil sloshing.

So liquid sloshing in tanks has been studied, both experimentally and theoretically, but only in tanks with simple stimulation. In this study, we explore the dynamics of liquid within an integrated tank that is stimulated not by external excitation but through a pump-valve assembly consisting of three water pumps. The concurrent operation of these pumps imposes enhanced dynamic forces on the liquid, inducing complex turbulent fluid motions.

Research into the mechanisms of liquid sloshing within such complex systems remains sparse, and few researchers have optimized the various parameters of baffles to restrain liquid sloshing in the tank and to suggest optimal solutions.

Our research aims to fill this gap by systematically analyzing and optimizing baffle parameters to better understand and control the sloshing phenomena in integrated tank systems. This work is crucial for improving the stability and efficiency of tank systems and can provide valuable insights for the design and operation of complex fluid systems. In this work, the coupled level-set and volume-of-fluid (CLSVOF) method is employed. It effectively captures various flow characteristics surrounding the baffle. The present study analyzes the impacts of baffle length, depth, and angle on fluid flow patterns and on the effectiveness of wave suppression within the tank. We propose a multi-criteria decision-making approach that incorporates wave height difference and air entrainment in the tank as independent objectives. The Kriging approximation method is employed to model the relationship between the design variables and the objectives. By utilizing the concept of Pareto optimality, we identify the solution that best meets the specified design requirements from the set of Pareto solutions. A new idea is provided for the structural design of integrated water tanks.

## 2. MATHEMATICAL MODEL

### 2.1 Geometrical Design

An integrated water tank is modeled using modeling software. The tank is made up of several components, including coolers and water pumps. A schematic diagram of the integrated water tank concept is given in Fig. 1(a). Its dimensions are as follows: height 285 mm, length 370 mm, width 380 mm. The water within the tank is recirculated back into the tank via a heat exchanger operated by a pump. In this study the pressure drop is regulated by using a porous medium, which serves to replicate the resistance encountered by fluid flow within a heat exchanger. Table 1 displays the tank parameters. A baffle is positioned within the tank, aligned parallel to the horizontal axis. The baffle is situated above the

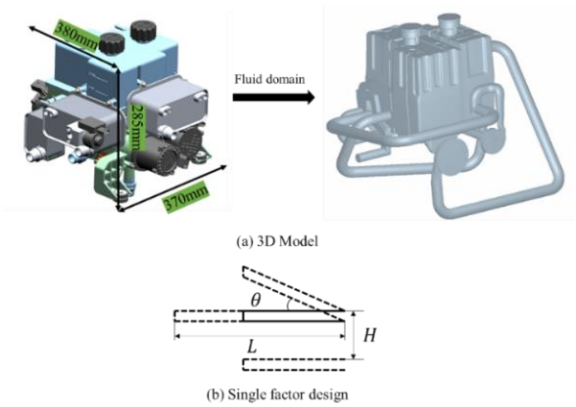


**Fig. 1 Schematic diagram of the model**

**Table 1 Variables used in analysis**

| Variable | Value |
|---|---|
| Pump speed (r/min) | 5500 |
| Tank volume (L) | 1.12 |
| Pressure drop in porous medium (KPa) | 52.3 |
| Porosity of porous medium | 0.75 |
| Particle diameter in porous medium (mm) | 7 |
| Initial liquid level (mm) | 245 |

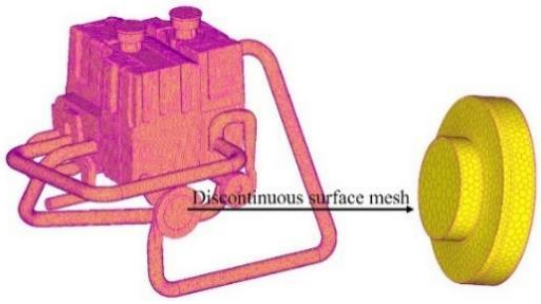


**Fig. 2 Mesh of fluid domain**

pump, which propels the fluid in an upward direction along the wall. This means that the baffle is strategically placed at the location where fluid sloshing is most pronounced. The dimensions of the baffle — its length ($L$), depth ($H$), and angle ($\theta$) — are depicted in Fig. 1(b). Fig. 2 graphically shows a mesh of the fluid domain.

### 2.2 Numerical Simulations

The liquid in the integrated tank whose sloshing is studied in this research is turbulent. Its mass conservation equation is

$$\frac{\partial \rho}{\partial \mathrm{t}}+\rho\left[\frac{\partial v_x}{\partial x}+\frac{\partial v_y}{\partial y}+\frac{\partial v_z}{\partial z}\right]=0 \tag{1}$$

and its momentum conservation equations are:

$$\rho\left[\frac{\partial v_x}{\partial t}+\frac{\partial v_x^{\,2}}{\partial x}+\frac{\partial v_x v_y}{\partial y}+\frac{\partial v_x v_z}{\partial z}\right]=-\frac{\partial p}{\partial x}+\frac{1}{\mathrm{Re}}\left[\frac{\partial \tau_{xx}}{\partial x}+\frac{\partial \tau_{xy}}{\partial y}+\frac{\partial \tau_{xz}}{\partial z}\right] \tag{2}$$

$$\rho\left[\frac{\partial v_y}{\partial t}+\frac{\partial v_x v_y}{\partial x}+\frac{\partial v_y^{\,2}}{\partial y}+\frac{\partial v_y v_z}{\partial z}\right]=-\frac{\partial p}{\partial y}+\frac{1}{\mathrm{Re}}\left[\frac{\partial \tau_{xy}}{\partial x}+\frac{\partial \tau_{yy}}{\partial y}+\frac{\partial \tau_{yz}}{\partial z}\right] \tag{3}$$

$$\rho\left[\frac{\partial v_z}{\partial t}+\frac{\partial v_x v_z}{\partial x}+\frac{\partial v_y v_z}{\partial y}+\frac{\partial v_z^{\,2}}{\partial z}\right]=-\frac{\partial p}{\partial z}+\frac{1}{\mathrm{Re}}\left[\frac{\partial \tau_{xz}}{\partial x}+\frac{\partial \tau_{yz}}{\partial y}+\frac{\partial \tau_{zz}}{\partial z}\right] \tag{4}$$

where, x, y, and z are distances in the three perpendicular directions, $v$ is velocity, and $\tau$ is shear stress.

The volume of fluid (VOF) method is employed to track the interface between different phases by iteratively solving for the volume fractions of the distinct fluids or phases inside the cell area at each time step. The VOF method represents each phase inside the model by using the cell phase volume fraction. It ensures that the total of the volume fractions of all phases within each control cell is equal to 1. The volume ratio of one of the phases, often the liquid phase (known as the target phase), to the overall cell volume is denoted as the volume function $F$

(sometimes known as the phase function) at each cell in a two-phase flow. For *F* there are three possibilities:

(1) F=0, gas phase

(2) F=1, liquid phase

(3) 0<F<1, element in mixed gas-liquid phase

The derivation of the convective transport equation for the phase function *F* may be accomplished in accordance with the rule of conservation of mass：

$$\frac{dF}{\mathrm{d}t}=\frac{\partial F}{\partial t}+\left(\vec{v}\cdot\nabla\right)F \tag{5}$$

where $t$ is time and $\vec{v}$ is the velocity vector. The density and viscosity of the fluid can be calculated as:

$$\rho=\rho_l F_l+\rho_g F_g \tag{6}$$

$$\mu=\mu_l F_l+\mu_g F_g \tag{7}$$

where $l$ and $g$ designate the liquid and gas phases, respectively.

The convection transport equation is instrumental in depicting the alterations in the phase function *F* driven by fluid dynamics. Specifically, it describes how the phase function evolves in response to velocity changes. Nonetheless, the phase function *F* exhibits discontinuities and cannot be smoothly differentiated near the phase boundaries. Consequently, direct application of the convection transport equation in the volume of fluid (VOF) model is not feasible. To address this challenge, it is imperative to devise a methodology for reconstructing the interface shape within grid cells that contain mixed phases. The approach for interface reconstruction varies, leading to different variants within the VOF model framework. These methodologies aim to mitigate issues such as solution oscillations and the smoothing over of abrupt parameter changes, which are pivotal for improving the accuracy of crucial physical calculations, including the determination of the normal direction and curvature at the phase interface.

The level-set function is a computational technique utilized for the purpose of interface tracking and shape modeling. The level-set function is a viable approach for conducting simulations of two-phase flow. It offers an effective means of capturing and describing the interfaces where the gas and liquid phases interact. This is achieved by the utilization of a smooth level-set function. This function Φ is employed to distinguish between different fluids, with the 0.5 contour of Φ serving as the boundary between air inflow (Φ = 0) and liquid inflow (Φ = 1). The movement of these fluids, characterized by a velocity ν perpendicular to the interface, can be mathematically described as the convective effect of the re-initialized level-set function, as expressed by the following equation:

$$\frac{\delta\Phi}{\delta t}+\left(\vec{v}\cdot\nabla\right)\Phi=0 \tag{8}$$

The convection transport equation of the phase function Φ reflects the displacement of the phase interface over time.

During this research, it was found that in certain situations when using the level-set method to solve the convection transport equation, the phase function Φ may lose its property as a distance function. If the computation continues without addressing this issue, incorrect results will be obtained. Typically, before the next step of computation, the phase function Φ needs to be reinitialized. However, during the transport and reinitialization process of the phase function Φ, strict adherence to the conservation of mass law cannot be guaranteed. This is the major drawback of the level-set method.

The presence of density, viscosity, and other flow-field factors can result in the formation of a discontinuity at the phase interface. Consequently, the position and morphology of the phase interface undergo alterations throughout the two-phase flow process, occasionally leading to fragmentation, polymerization, and other related phenomena. Furthermore, the exchange of mass, momentum, and energy between the two phases occurs via the phase interface. Therefore, precise monitoring of the phase interface is crucial for the numerical computation of two-phase flow and serves as a requirement for solving its governing equations. The flow pattern observed in the integrated tank during two-phase flow exhibits a wave-like oscillatory behavior. As the pump propels the liquid to circulate within the tank, the fluid undergoes oscillatory flow due to the influence of inertial forces (Albadawi et al., 2013).

The volume of fluid (VOF) method is characterized by its straightforward computational process and the notable sharpness of the phase interface. However, it is important to note that the fluid volume function associated with this method exhibits discontinuities at the phase interface. Consequently, this discontinuity results in abrupt changes in fluid parameters, thereby smoothing out oscillations and leading to inaccuracies in the calculation of the normal direction of the phase interface, as well as the curvature and other related physical quantities. Hence, the incorporation of the level-set function into the VOF method, specifically known as the couple level-set volume of fluid (CLSVOF) method, is proposed. This approach employs the distance function provided by the level-set function to accurately track the continuity of the phase interface. By doing so, it aims to address the inaccuracies associated with parameters such as the curvature of the phase interface, the normal vector, and the surface tension during the computation of two-phase oscillatory flow in an integrated tank. Consequently, this integration of the level-set function enhances the precision of numerical calculations pertaining to the two-phase flow field within the integrated tank. The CLSVOF method utilizes the "values" associated with the VOF and level-set functions to simultaneously recreate the interface.

The coupled level-set and volume of fluid (CLSVOF) method has been developed to address the inherent limitations of the traditional VOF method, particularly in precisely calculating parameters such as the normal vector and curvature, and in resolving the mass conservation issue associated with the level-set function. This enhancement significantly increases the accuracy of

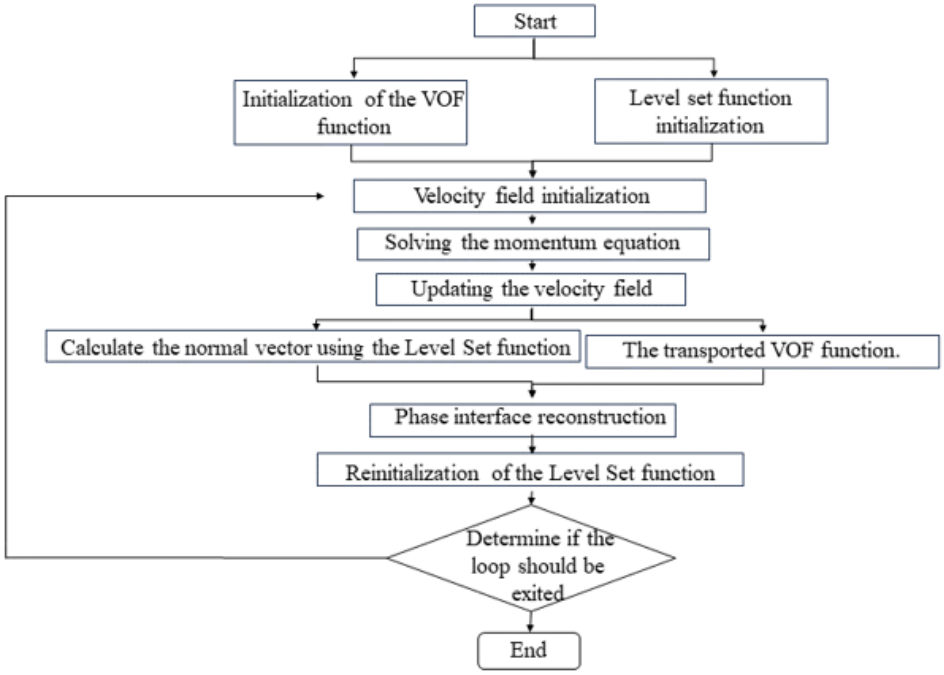


**Fig. 3 CLSVOF method flowchart**

numerical simulations concerning two-phase oscillatory flow in integrated water tanks. In the CLSVOF approach, both the VOF and level-set functions are employed concurrently to reconstruct the fluid interface. Here, the volume fraction of the liquid phase in the VOF model specifies the location of the interface, whereas the direction of the interface gradient is ascertained using the level-set function through geometric techniques. This dual-function strategy helps in fine-tuning the interface capturing process to significantly reduce interface diffusion, thereby improving the fidelity of the simulation. The methodological workflow for tracking the phase interface using the CLSVOF method is detailed in the flowchart in Fig. 3. This flowchart outlines the steps taken to ensure precise and robust interface tracking, critical for achieving reliable and accurate computational results in complex fluid dynamics scenarios.

The VOF model utilizes the volume fraction of the liquid phase to establish the value of the interface. At the same time, the direction of the gradient at the interface is determined by geometric approaches using the level-set function. This interface-capture approach employs many strategies to ensure that the interface does not expand. However, in order to see and effectively analyze tiny phenomena such as water droplets and bubbles, it is necessary to improve the spatial resolution to a significant degree. Hence, the analysis of these events utilizing the interface capture approach may provide challenges in terms of processing costs. To tackle these issues, the fine interface reconstruction technique (FIRM) was devised. The piecewise-linear interface calculation (PLIC) approach, commonly employed for structured meshes, is adapted for the purpose of handling unstructured meshes in the FIRM framework. In the context of PLIC, the quantification of advective fluid is determined using meticulous geometric calculations, resulting in highly accurate outcomes. The regulations are outlined as follows:

（1）The determination of the interface's normal orientation in each cell is achieved by analyzing the distribution of the VOF data.

（2）The position of the free surface in each cell is determined by utilizing the interface normal direction and the VOF value that has been received. The interface is assumed to be flat.

（3）The volume of liquid advected into neighboring cells is calculated based on the free surface positions and cell interface velocities obtained in Step 2.

（4）The VOF value of the element is updated by considering the volume of liquid that flows in or out of the element interface.

The integration of multiple pipes flowing through the components in an integrated water tank is extremely complex. Therefore, in our model, we simplify the piping system and focus on the areas where heat exchangers and condensers are located. We use a porous medium to simulate the flow resistance experienced by the fluid passing through this region. In this study, we select solid particles as the filling material for the porous medium. The porosity, particle diameter, and shape factor are chosen as characteristic variables for the porous medium. If the porous medium is composed of spherical particles, the contact area per unit volume of particles can be calculated using the following equation:

$$\frac{A_P}{D_P}=\frac{\pi D_P^2}{\pi D_P^3/6}=\frac{6}{D_P} \tag{9}$$

In this equation, $D_P$ represents the particle diameter. We introduce a correction factor for non-spherical particles:

**Table 2 Grid independence test**

| Grid number(thousand) | 300 | 550 | 800 | 1050 | 1300 |
|---|---|---|---|---|---|
| Monitoring points | | | | | |
| Point1(m/s) | 0.162 | 0.181 | 0.231 | 0.232 | 0.230 |
| Point2(m/s) | 0.081 | 0.121 | 0.148 | 0.150 | 0.155 |
| Point3(m/s) | 0.062 | 0.112 | 0.162 | 0.161 | 0.164 |

**Table. 3 Time step independence test**

| Time step(s) | 0.0005 | 0.0003 | 0.0001 | 0.00005 | 0.00003 |
|---|---|---|---|---|---|
| Monitoring points | | | | | |
| Point1(m/s) | 0.251 | 0.246 | 0.234 | 0.232 | 0.230 |
| Point2(m/s) | 0.168 | 0.161 | 0.152 | 0.154 | 0.153 |
| Point3(m/s) | 0.172 | 0.170 | 0.16 | 0.161 | 0.164 |

$$\frac{A_P}{D_P} = \frac{6}{\Phi_C D_P} \tag{10}$$

In this equation, $\phi_C$ represents the particle shape factor. The contact area ratio per unit volume is expressed as:

$$X = \frac{6}{\Phi_C D_P}(1-\varepsilon) \tag{11}$$

The pressure drop per unit distance along the flow direction is given by the following relationship:

$$F = \frac{6 f U^2 \rho_l (1-\varepsilon)}{\Phi_C D_P \in^2} \tag{12}$$

$$f = \begin{cases} \dfrac{5}{\mathrm{Re}} (\mathrm{Re} < 2) \\ \dfrac{5}{\mathrm{Re}} + \dfrac{0.4}{\mathrm{Re}^{0.1}} (2 \le \mathrm{Re}) \end{cases} \tag{13}$$

$$\mathrm{Re} = \frac{\Phi_C D_P U \rho_l}{6(1-\in)\mu_l} \tag{14}$$

In these equations, $U$ is the average velocity (m/s), $\rho_l$ is the fluid density (kg/m³), $\epsilon$ is the porosity, $D_P$ is the particle diameter (m), and $\mu_l$ is the fluid viscosity ($Pa \cdot s$).

Due to the coupling of the level-set function and the volume of fluid (VOF) method, the CLSVOF approach exhibits a higher degree of computational complexity, potentially necessitating increased computational resources and time. Furthermore, the accuracy and stability of the CLSVOF method are influenced by the chosen grid, with coarser grids introducing higher levels of error into the simulation results. To tackle these challenges, offsetting strategies were implemented in this study. First, diligent efforts were made to minimize the simulation time as much as possible. Second, a thorough analysis of grid dependency was conducted to determine the optimal number of grid cells.

To test the grid independence, simulations were performed using 300, 550, 800, 1050, and 1300 thousand grid numbers. A baffle length ratio of 2, a baffle-to-free-surface-distance of 0 and a baffle angle of 0 are used as the parameters of the test conditions for measuring the grid independence. The instantaneous velocities at the monitoring points in the tank (Fig. 4) were compared and the calculation results, shown in Table 2, revealed that when the mesh size is increased from 300 to 800 thousand, the maximum velocity change is about 0.1 m/s. When the number of meshes is increased to 1300 thousand, the maximum velocity change is less than 0.01 m/s and the relative error is within 0.03%. Thus, according to the simulation calculations, in order to reduce the time cost while ensuring sufficient computational accuracy, a mesh number of 800 thousand was chosen (Stern et al., 2006).

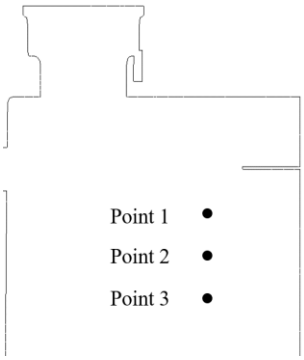


**Fig. 4 Independence Verification Monitoring Points**

The time step sizes are 0.0005, 0.0003, 0.0001, 0.00005, and 0.00003 seconds for the independence verification of the time step size. As shown in Table 3, as the time step size decreases, the instantaneous velocity variations at the three monitoring points all become smaller and smaller. Therefore, it can be estimated that the instantaneous velocity stabilizes at a time step size of 0.0001 seconds. If the step size is too small, it will significantly increase the computational time, and if it is too large, it will diminish the accuracy of the calculation. In this study, the computational time step size is set to 0.0001 seconds.

### 2.3 Numerical Validation

This study aimed to assess the flow resistance within the integrated water tank through the utilization of a test

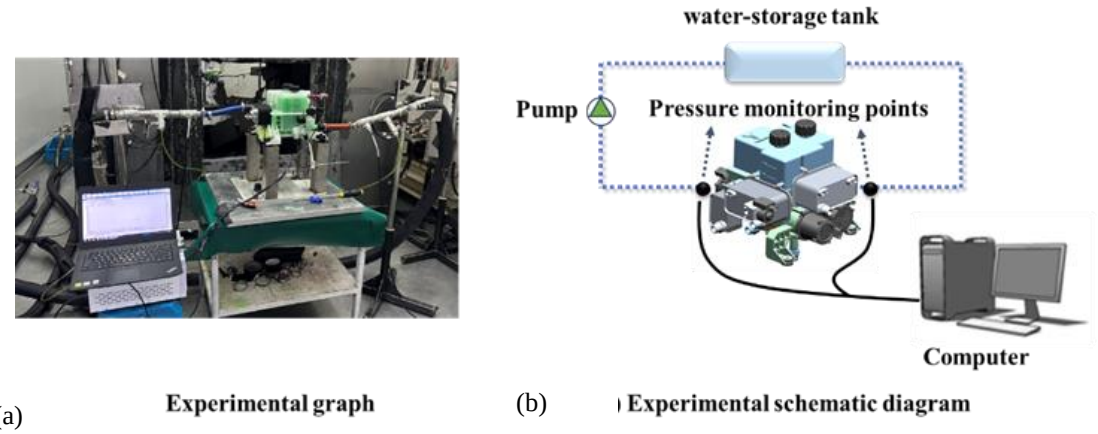


**Fig. 5 The experimental setup**

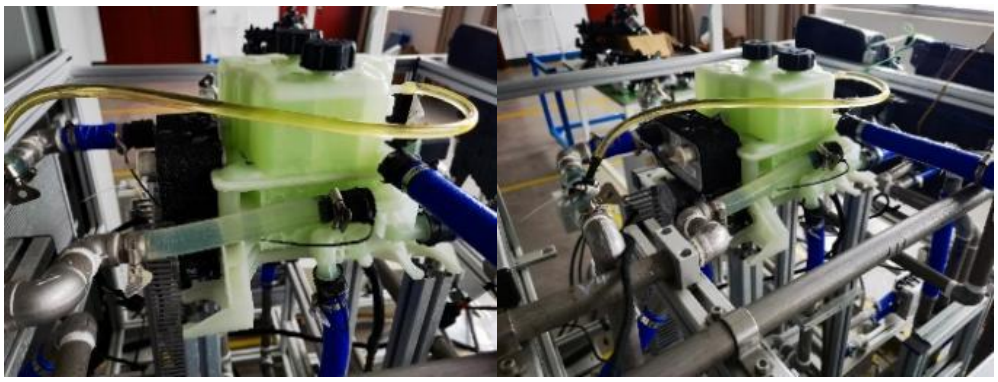

**Fig. 6 The experimental setup**

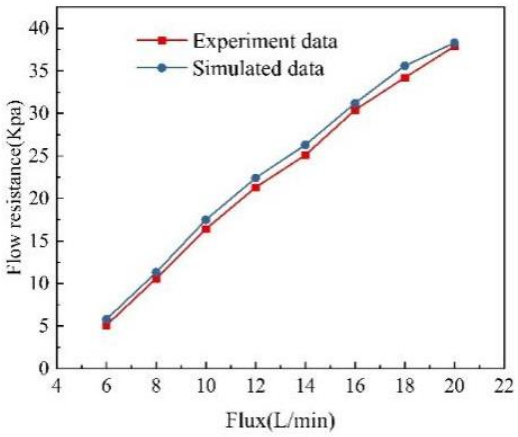


**Fig. 7 Comparison of the experimental and simulated results**

setup. The construction of the system bench necessitated ensuring that the input and exit of the cooling water circuit align with the overall preservation of the vehicle. The coolant inlet pressure test point of the cooling water circuit is located at 40 ±10 mm from the coolant inlet of the object being tested. Similarly, the outlet pressure test point is situated at 40 ± 10 mm from the coolant outlet of the object under test. The water temperature is measured to be 20 ℃ under ambient conditions, while the flow rate ranges from 6 to 20 L/min. A pressure sensor is utilized to assess the outlet and intake pressures of the cooling water circuit. The schematic layout of the experimental apparatus is shown in Figs. 5 and 6. An objective of this study is to measure the resistance of the independent circuit flow in the integrated water tank. The results depicted in Fig. 7 demonstrate strong agreement between the simulated flow resistance and the experimental findings. This correspondence suggests that the simulation model employed in the study is valid and reliable.

### 2.4 Numerical Procedure

The simulation findings are influenced mostly by the density and viscosity of both the gas and liquid phases, as observed during the investigation. The density and viscosity values for the gas phase, namely air, are reported as 1.29 kg/m$^3$ and 0.01809 mPa·s, respectively. On the other hand, the density and viscosity values for the liquid phase, specifically liquid water, are documented as 998.2 kg/m$^3$ and 1.005 mPa·s, respectively. The utilization of a computational fluid dynamics (CFD) solver is employed for the numerical resolution of the governing equations. The issue at hand is regarded as a transient turbulence problem, employing a first-order explicit time discretization and a second-order windward space discretization. The gradient term is expressed in the format of least squares cell, while the pressure term is represented in the format of second order interpolation. The turbulent energy is resolved by the utilization of the second-order windward approach. A convergence threshold of $10^{-5}$ is

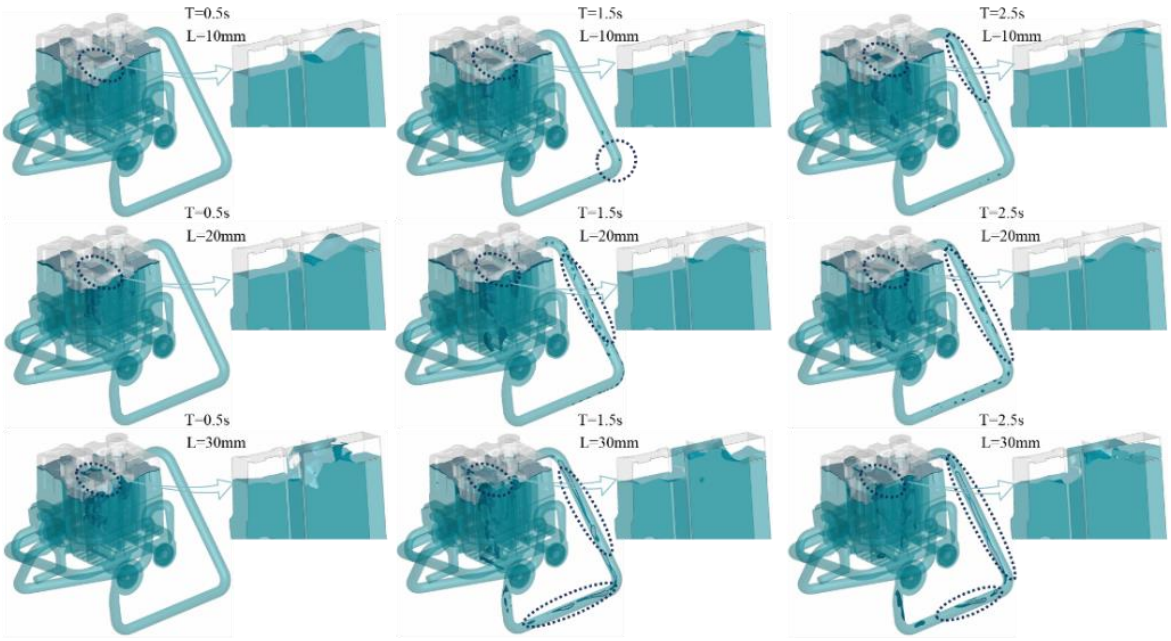


**Fig. 8 Two-phase flow distribution with different baffle lengths**

employed for every residual component. The transient simulation in this work employs a time step of 0.0001 s and is executed for a total of 25,000-time steps. The whole duration of the simulation is 2.5 seconds.

## 3. SINGLE-FACTOR ANALYSIS

### 3.1 Effects of Baffle Length

The baffle depth is established at the initial liquid level, with the vertical wall positioned at a 0° angle. The length of the baffle is then adjusted in order to investigate the impact of varying baffle lengths on the prevention of liquid sloshing within the tank. Fig. 8 illustrates the distribution of two-phase flow throughout the integrated tank, with a specific focus on the magnified view of the two-phase flow occurring in the baffle zone. According to the Fig. 4, it is evident that variations in the baffle length have resulted in diverse alterations in the liquid level within the water tank. The parameter η is defined as the disparity between the maximum amplitude of the wave in the tank and the beginning height of the liquid level. The disparity in liquid level heights is seen in Fig. 9 for various lengths of baffles.

Based on the results of data analysis, it is seen that the enhancement of the liquid level height suppression effect in the tank does not exhibit a positive correlation with the increase in baffle length. Surprisingly, the optimal wave height suppression effect in the tank was achieved when the baffle length was 20 mm. Based on the analysis of the phase distribution graph and the wave height difference data graph, it is seen that when the baffle length is set at 30 mm, the liquid impact on the top of the tank occurs within the time interval of 0.5 to 2.5 s.

The reason for this phenomenon is the excessive length of the baffle, which results in a decrease in the gap between the baffle and the inner wall of the tank. The pump drive exerts pressure on the liquid, resulting in a

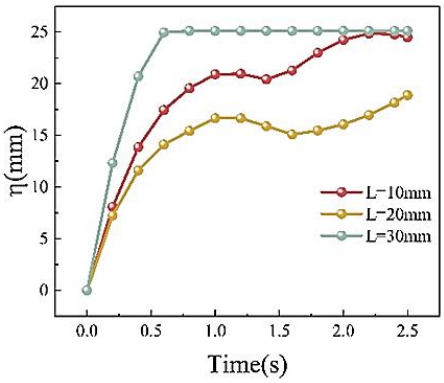


**Fig. 9 The relationship between distinction and t in the wave height for different baffle lengths**

rapid alteration in its velocity. This abrupt change in velocity induces vigorous motion at the top the tank, leading to collisions with the baffle. The wave height suppression effect is less pronounced when the baffle length is 10 mm than when it is 20 mm. The incomplete coverage of the water kinetic energy area by the baffle length inhibition range results in the retention of a portion of the liquid water's kinetic energy that remains unconsumed by the baffle.

The study additionally found that an increase in the size of the tank cycle's baffle led to the generation of air bubbles in the tank pipework, resulting from the two-phase flow distribution field within the tank. The negative pressure created by the pump facilitates the movement of air from within the tank into the pump, as the liquid is being transferred.

The aggregate quantity of air bubbles that are introduced into the pump region for a time interval of 2.5 seconds, as depicted in Fig. 10, The quantity of air that was entrained and drawn into the water tank remained

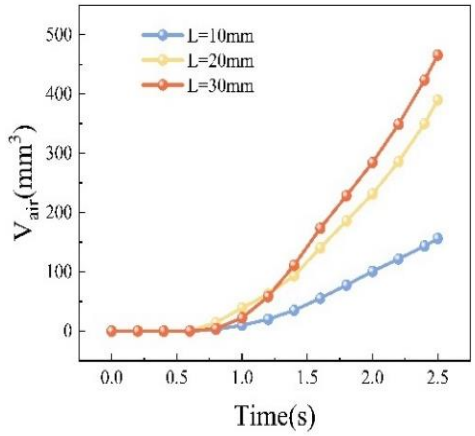


**Fig. 10 The relationship between distinction and t in the volume of air for different baffle lengths**

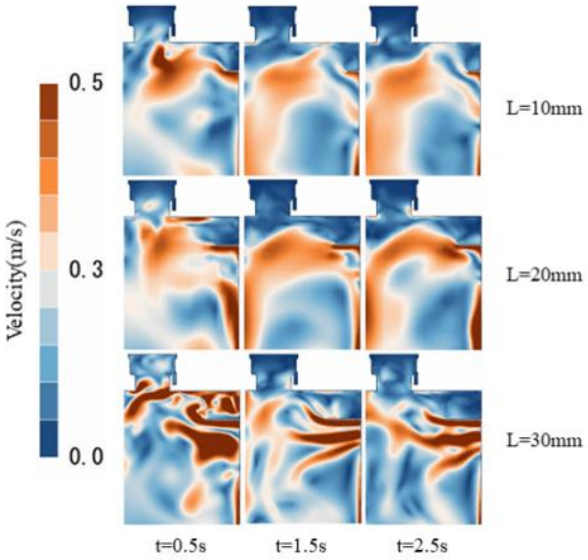


**Fig. 11 The velocity distribution of liquid in a tank with different baffle depths**

exceptionally stable until the 0.5-second mark. Over time, there has been an increase in the air volume within the water pump. When the length of the baffle is set to 30mm, the maximum volume of air breathed inside its pump area is recorded as 465.74mm$^3$. This phenomenon occurs due to the presence of a 30mm baffle length, resulting in vigorous agitation of the liquid within the tank. Consequently, this agitation hinders the generation of impact forces on the top surface of the tank. Additionally, the agitation causes the liquid to fragment, leading to the incorporation of air into the liquid phase.

Concurrently, the baffle exerts a compressive force back onto the liquid, amplifying the liquid's velocity and generating an upward thrust. This thrust pushes the liquid upwards, so that the liquid ascends towards the tank's upper regions, thereby creating a marked difference in liquid-level height. Furthermore, the impact of the liquid against the baffle not only increases velocity but also causes the liquid to fragment and become more dispersed, which in turn facilitates the entrainment of air into the liquid. Consequently, as the baffle length increases, so too does the amount of air that becomes entrained within the liquid. This detailed analysis underscores the complex interplay between baffle configuration and fluid dynamics within the tank.

Figure 11 illustrates the velocity distribution of liquid within a tank equipped with baffles of varying lengths. It is apparent from the analysis that reducing the length of the baffle leads to an increase in liquid velocity in the tank's left half. Notably, when the baffle length is set to 30mm, the velocity near the baffle is significantly elevated compared to the scenarios with baffle lengths of 10mm and 20mm. This phenomenon can be attributed to the fact that a longer baffle interacts with a greater volume of liquid, which leads to more frequent and intense collisions at the baffle surface. Such interactions cause abrupt changes in velocity as the liquid strikes the baffle. Concurrently, the baffle exerts a compressive force back onto the liquid, amplifying the liquid's velocity and generating an upward thrust. This thrust pushes the liquid upwards, the liquid ascends towards the tank's upper regions, thereby creating a marked difference in liquid level height. Furthermore, the impact of the liquid against the baffle not only increases velocity but also causes the liquid to fragment and become more dispersed, which in turn facilitates the entrainment of air into the liquid. Consequently, as the baffle length increases, so too does the amount of air that becomes entrained within the liquid. This detailed analysis underscores the complex interplay between baffle configuration and fluid dynamics within the tank.

### 3.2 Effects of Baffle Depth

The length of the baffle was configured to be 20 mm and positioned vertically against the wall, resulting in an angle of 0° for the baffle. This study aimed to evaluate the impact of varying baffle depths on the mitigation of liquid sloshing within the integrated tank. The depths of the baffles were established at three specific locations relative to the original free surface. These locations were at the free surface itself (H=0mm), 40mm below the free surface (H=40mm), and 80mm below the free surface (H=80mm).

Figure 12 illustrates the progression of the distribution of two-phase flow for various baffle depth settings at different time intervals. It is evident that as the depth of the baffle increases, the changes in the free surface become less pronounced. At a height of 80 mm, the free surface exhibits a single wave crest. The examination of the data on wave height difference, as depicted in Fig.13, reveals that the reduction in wave height difference is most prominent at a height of 80 mm, with a subsequent decrease observed at zero depth. This is due to the proximity of the baffle to the pump, positioned at 80 mm from the initial liquid level. Baffles are utilized to alter the trajectory of liquid flow, hence enhancing the dissipation of liquid energy. This modification prevents the liquid from impacting the free surface with excessive velocity during its upward travel. When the baffle is positioned 40 mm away from the initial liquid level, the liquid's kinetic energy resulting from the pump drive is greater at this specific distance. While it is flowing in an

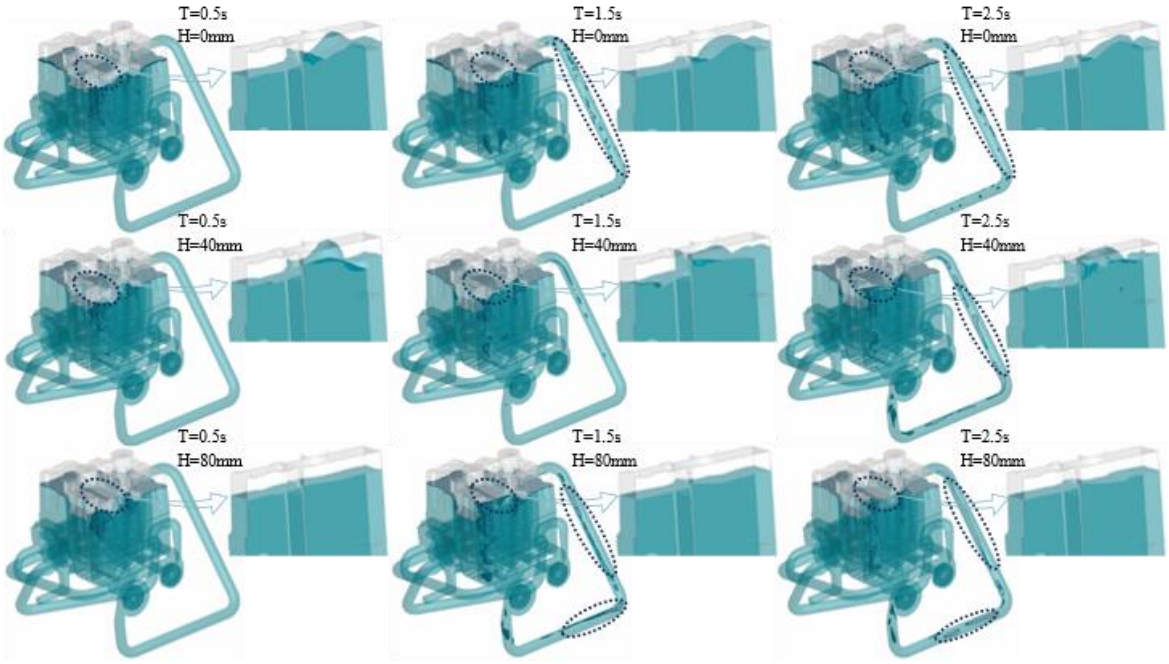


**Fig. 12 Two-phase flow distribution with different baffle depths**

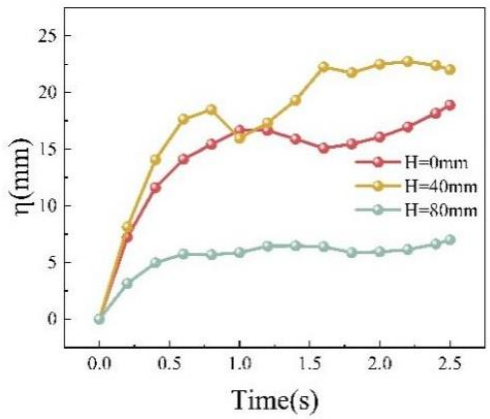


**Fig. 13 The relationship between distinction and t in the wave height for different baffle depths**

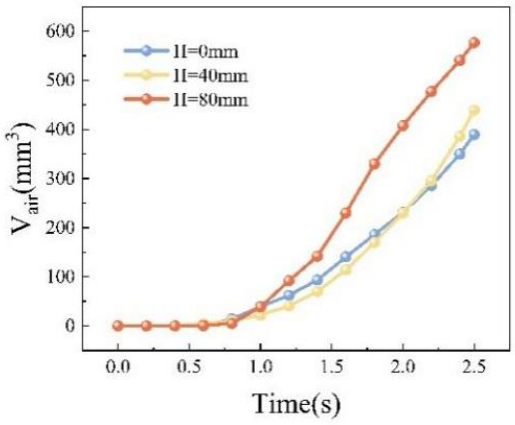


**Fig. 14 The relationship between distinction and t in the volume of air for different baffle lengths**

upward direction, the presence of a baffle restricts the dissipation of kinetic energy, resulting in a greater magnitude of oscillations.

Despite the fact that the 80-mm baffle in the tank effectively inhibits liquid sloshing, the study of the total air volume in the pump region reveals that it has the largest volume inhalation of 576.81mm$^3$, as seen in Fig. 14, The observed phenomenon may be attributed to the presence of a baffle within the inner cavity of the tank adjacent to the pump. This baffle contributes to an increased flow resistance within the tank, thus leading to an elevation in negative pressure. The ingress of air into the liquid and subsequent rolling into the pump is not a result of the liquid being compressed, but rather a consequence of the excessive negative pressure, which causes the air to be drawn into the liquid and afterwards rolled into the pump. There is no substantial disparity between the volume of air introduced at the 40-mm depth of the tank and that at the initial surface of the baffle.

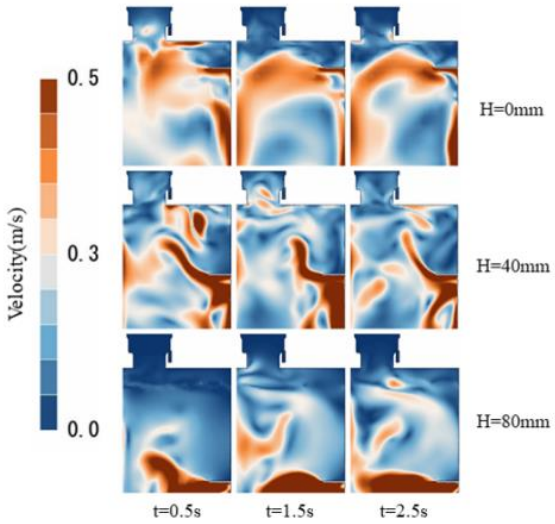


**Fig. 15 The velocity distribution of liquid in a tank with different baffle depths**

Figure 15 presents the velocity distribution of liquid in a tank with baffles of varying depths. It has been observed

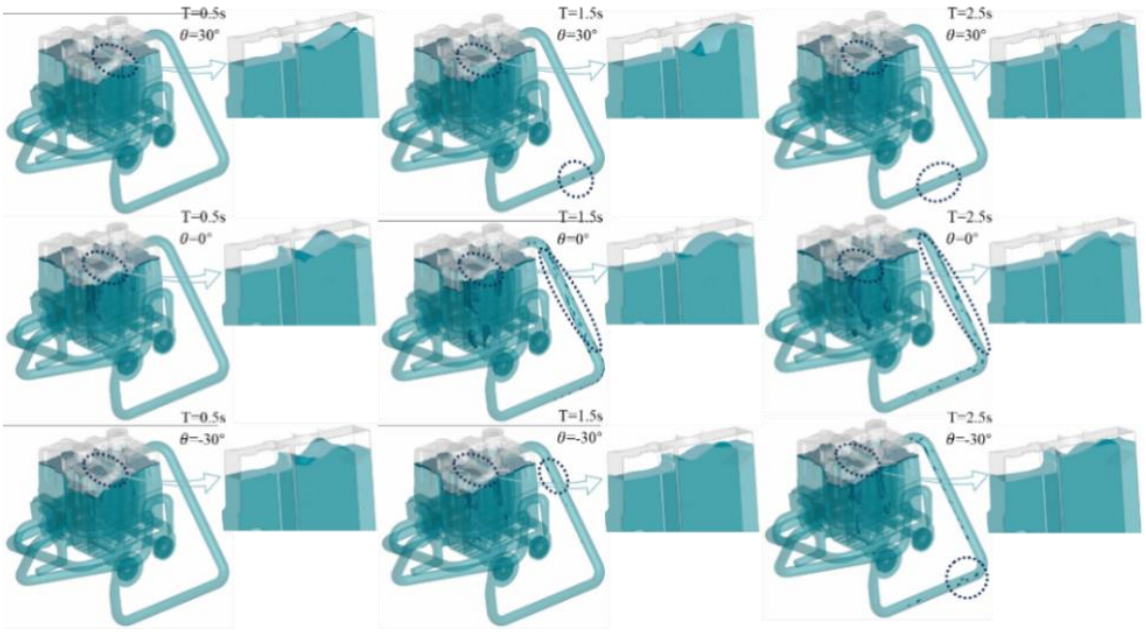


**Fig. 16 Two-phase flow distribution with different baffle angles**

that increasing the baffle depth causes the droplet velocity clusters within the tank to move downward, while simultaneously decreasing the velocity of the liquid in the upper layer of the tank. Notably, independent of the baffle depth, there is consistently a prominent velocity cluster near the bottom of the baffle, and this cluster's size expands as the baffle depth increases. This pattern suggests that a greater baffle depth effectively dampens the motion of the liquid above the baffle, restricting higher velocities to the area below the baffle. Consequently, the velocity distribution data allow us to conclude that an increase in baffle depth acts as a robust mechanism for reducing variability in liquid levels within the tank, as corroborated by the associated analysis of liquid level differences. Moreover, the downward migration of velocity clusters observed with increased baffle depth results in heightened flow resistance inside the tank and a corresponding rise in vacuum pressure. This change in dynamics leads to greater air entrainment by the liquid and subsequently into the water pump system. Therefore, while a baffle depth of 80 mm is identified as most effective in minimizing liquid level disparities, it also coincides with the maximum air entrainment observed, illustrating a trade-off between suppressing liquid level differences and the potential for increased air intake.

### 3.3 Effects of Baffle Angle

The baffle angle, denoted $\theta$, was adjusted within the range of -30° to 30° at the initial free surface of the tank. The length of the baffle was established to be 20 mm. Fig. 16 illustrates the variations in the free surface across several time intervals, corresponding to varying configurations of the baffle angle. The rate of change of the free surface during the time interval of 0.5 to 2.1 s exhibits a reduction when the baffle angle declines. Additionally, when the baffle angle is set at 30°, the free surface experiences rolling absorption above the baffle. Examination of the data on wave height difference (Fig.

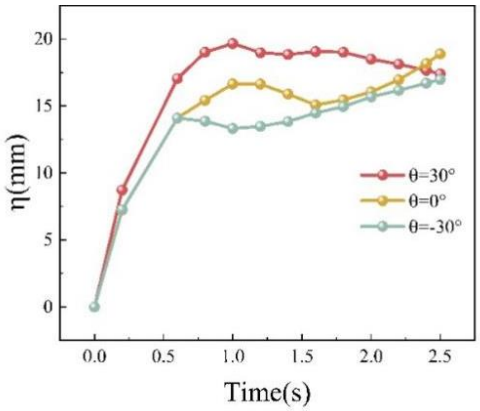


**Fig. 17 The relationship between distinction and t in the wave height for different baffle angles**

17) indicates that the baffle exhibits optimal efficacy in mitigating wave-height difference at a baffle angle of 30°, while it is least effective in reducing wave height difference at a baffle angle of -30°. This phenomenon occurs because the inclination of the baffle at an angle of 30° causes the liquid to move in an upward direction. It is important to note that the baffle angle does not forcefully alter the direction of liquid movement, thus the inhibition of hydrokinetic energy is not pronounced. However, the liquid movement tends to become more nearly horizontal. After a duration of 1.5 sec, liquid enters the top portion of the baffle, effectively preventing liquid agitation and enhancing the dissipation of energy within the liquid. With a baffle angle of -30°, the direction of liquid movement is compelled to shift from upward to downward, resulting in an augmented dissipation of kinetic energy in the water. Additionally, as the liquid within the tank moves upward and encounters the baffle, its impact with the baffle is responsible for a significant reduction in its kinetic energy.

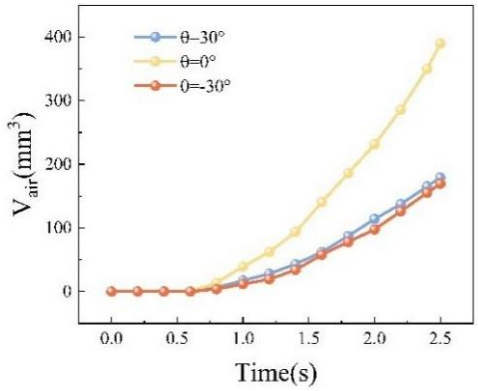


**Fig. 18 The relationship between distinction and t in the volume of air for different baffle angles**

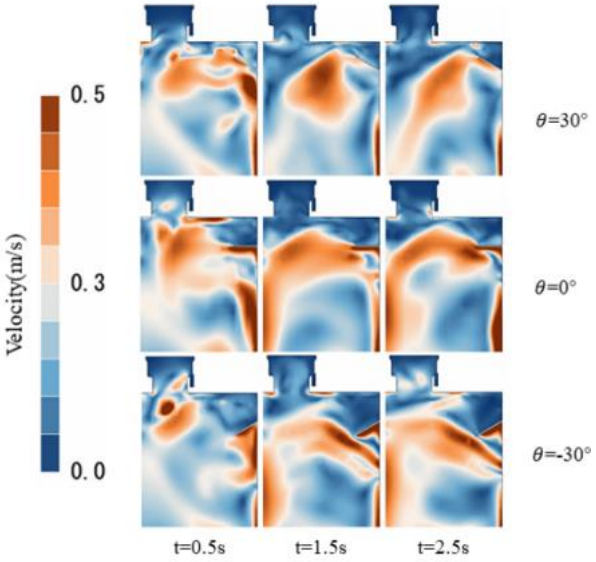


**Fig. 19 The velocity distribution of liquid in a tank with different baffle angles**

Modifying the baffle angle demonstrates a more pronounced impact on the diminution of air roll suction in comparison to its very limited influence on the discrepancy in wave height within the tank. When the baffle is positioned at an angle of 30° or -30°, the volume of air-bubble suction in the pump region decreases to 179.24 $mm^3$ and 169.31 $mm^3$ (Fig. 18), respectively. When the angle is 30°, the liquid's velocity is directed horizontally, and there is no vigorous vertical motion. Consequently, air bubbles are predominantly found close to the free surface, with minimal entrapment within the pump. In the case of an angle of -30°, it is seen that the liquid exhibits vigorous vertical motion. However, a phenomenon of hedging occurs, in which the upward movement of the liquid counteracts the upward motion of air bubbles. Consequently, only a limited number of air bubbles are present in the water tank.

Figure 19 illustrates the velocity distribution of liquid in a tank with baffles set at various angles. The analysis indicates minimal variation in liquid velocity for different baffle angles, suggesting that the angle of the baffle has a relatively moderate impact on the height difference in the liquid levels. This observation is consistent with the liquid level difference analysis, which confirms the subdued influence of baffle angle on suppressing vertical liquid displacement. In terms of air entrainment, the study finds that certain baffle angles are more effective at reducing air intake than configurations with no angle adjustment. Specifically, at a 30° baffle angle, the liquid ascends along the baffle smoothly, avoiding harsh collisions. This gentle interaction prevents the liquid from breaking apart, thus minimizing air entrainment. In contrast, at a 0° angle, the liquid strikes the baffle directly, resulting in vigorous splashing and increased air entrainment due to the fragmentation of the liquid. Moreover, with a -30° baffle angle, although the liquid still collides and breaks apart upon impact with the baffle, an eddy current forms beneath the baffle. This vortex helps dissipate some of the liquid's kinetic energy, leading to a more tranquil state within the tank and comparatively less air entrainment than is observed in the other two scenarios. This analysis elucidates how different baffle angles influence the tank's internal dynamics, particularly concerning air entrainment and liquid level stability.

## 4. OPTIMIZATION OF THE COOLING STRUCTURE

### 4.1 Kriging Approximate Model

Construct an approximation model utilizing the Kriging model to examine the influence of the baffle length, depth, and angle on both wave height and air volume. The functional connection between the dependent variable and the independent variable in the model may be mathematically represented by the following equation:

$$\tilde{Y}\left(X_0\right)=\sum_{i=1}^{n}\lambda_i Y_i\left(X_i\right) \tag{15}$$

where $\tilde{Y}(X_0)$ is the predicted value of the unidentified data point， $X_0$is the unidentified data point; $X_i$ is the identified data point, $and\ \lambda_i$ is the required weighting factor.

### 4.2 Design of the Scheme

The Latin hypercube sampling method is employed to design various parameters, ensuring that the sample points inside the design space are uniformly distributed. This paper examines the relationship between three factors. For the Kriging model, we determine the number of sample sites using the $N \geq 2n + 1$ formula. There are at least seven sample points. The more data that is fed into the model, the better it will perform. However, getting the sample data takes more time. The study uses a total of 18 sample points, chosen with an emphasis on precision and ease of execution. Upper and lower limits of the three dimensions are established based on the tank size and single-factor analysis of the structure with the baffles; they are stated in Table 4 (Baodong et al., 2011).

**Table. 4 Upper and lower limits of the three dimensions**

| Factors | Upper value | Lower value |
|---|---|---|
| L(mm) | 10 | 30 |
| H(mm) | 0 | 80 |
| θ(°) | -30 | 30 |

**Table 5 Design scheme and calculation results**

| Scheme | Design variables | | | Object function | |
|---|---|---|---|---|---|
| | L/mm | H/mm | θ/° | Vair/mm$^3$ | $\eta$/mm |
| 1 | 28 | 28 | 0 | 77.34 | 15.44 |
| 2 | 22 | 66 | 30 | 230.31 | 14.04 |
| 3 | 17 | 33 | -21 | 87.10 | 16.039 |
| 4 | 15 | 9 | 25 | 202.43 | 19.62 |
| 5 | 20 | 26 | 22 | 120.27 | 11.923 |
| 6 | 30 | 16 | 12 | 104.24 | 12.872 |
| 7 | 14 | 20 | -26 | 84.69 | 17.935 |
| 8 | 16 | 52 | 8 | 93.06 | 18.382 |
| 9 | 25 | 74 | 6 | 211.21 | 9.43 |
| 10 | 10 | 78 | -11 | 119.52 | 14.801 |
| 11 | 12 | 0 | -6 | 143.16 | 19.335 |
| 12 | 27 | 42 | 16 | 82.53 | 17.177 |
| 13 | 19 | 36 | -3 | 107.44 | 18.026 |
| 14 | 23 | 69 | -16 | 146.97 | 3.542 |
| 15 | 29 | 56 | -30 | 219.62 | 6.738 |
| 16 | 20 | 47 | -17 | 117.68 | 11.921 |
| 17 | 25 | 7 | -9 | 106.15 | 13.576 |
| 18 | 12 | 59 | 20 | 181.32 | 10.265 |

The Latin hypercube sampling method was used to find 18 distinct structures. The simulation determined the wave length difference η and the volume of air $V_{air}$ using these models. The outcomes are detailed in Table. 5.

### 4.3 Multi-Objective Optimization of Baffles

The design plan is optimized by the utilization of the multi-objective genetic algorithm NSGA-II using the MODELFRONTIER software. Genetic algorithms simulate the process of natural selection by replicating the evolutionary dynamics observed in animals, so enabling adaptation to the principle of survival of the fittest. The optimization index can be achieved by iterative refinement of alternative solutions. In the context of multi-objective optimization, it is common for the values of the associated decision variables to diverge when the objective function reaches its optimal state. The other objective functions will deviate from the optimal value when one of them attains an ideal value. A Pareto solution refers to a solution that achieves optimal performance in the objective function without compromising the performance of other objective functions. Figure 20 depicts the spatial arrangement of Pareto solutions inside the design-variable space. The set of iterative solutions is denoted by black dots, whereas the set of Pareto solutions is denoted by blue dots. The utilization of the MODELFRONTIER software enables users to select solutions from Pareto solution sets that meet design requirements through the application of multi-criteria decision-making (MCDM) techniques. This method prioritizes the Pareto solutions by assigning weights to each objective function, which are adjusted based on actual needs. Both reducing the volume of air taken in and decreasing the wave height in the tank are essential objectives. Consequently, within the scope of this inquiry, the parameters assigned to the weight of air intake and the disparity in wave height are both established at a value of 0.5. The Pareto solution can be employed to ascertain the optimal solution. The numerical simulation was repeated using the optimized design variables (*L*, *H*, and $\theta$) to validate the results obtained from the optimization process.

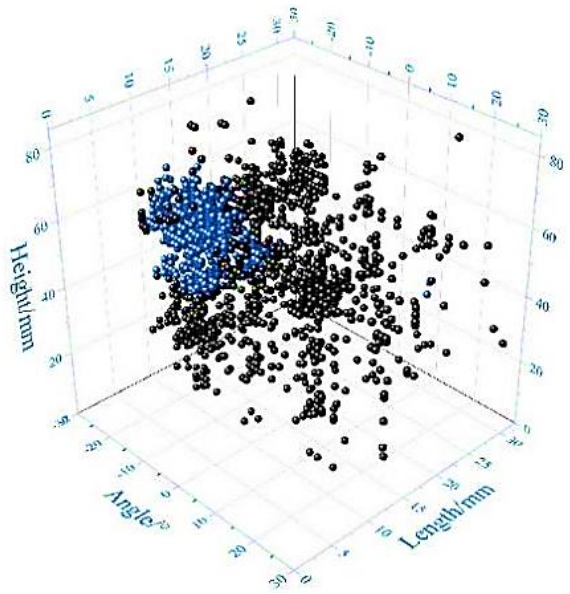


**Fig. 20 Pareto solution distribution in the design variable space**

The results are presented in Table. 4. The data shown in Table. 6 demonstrates that the multi-objective optimization strategy frequently yields accurate outcomes, since the best solution closely aligns with the computational fluid dynamics (CFD) results.

## 5. CONCLUSIONS

This study is based on the coupled CLSVOF method for numerical simulation. The control variable method was used to investigate the variation of liquid flow inside the integrated tank by changing the parameters of the three

**Table 6 Optimized solution and numerical simulation by CFD**

| Design | Optimal solution | CFD result | Error/ % |
|---|---|---|---|
| L/mm | 13 | 13 | |
| H/mm | 49 | 49 | |
| $\theta$/° | -20 | -20 | |
| Objective function | | | |
| $\eta/mm$ | 17.91 | 16.35 | 8.7 |
| Vair/mm$^3$ | 54.22 | 52.1 | 3.9 |

factors influencing the baffle. The effects of different structural parameters on the suppression of liquid sloshing inside the integrated tank were then compared by analyzing the two-phase flow evolution, wave-height difference, air-roll suction volume, and the velocity distribution. By taking the baffle length ($L$), baffle depth ($H$), and baffle angle ($\theta$) as optimization variables and minimizing the wave height difference ($\Delta\eta$) and air roll suction volume ($V_{air}$) as optimization objectives, response surface approximation models were established for each optimization objective. Finally, the optimal structural parameters were obtained through optimization and were validated. The specific conclusions are as follows:

1. A baffle structure was proposed and analyzed through a single-factor simulation which showed that the free surface height inside the tank decreases linearly as baffle length increases. Furthermore, increasing the distance between the baffle and the initial free surface leads to a significant reduction in surface height. Elevating the baffle angle also lowers the free surface height within the tank. Notably, a baffle depth of 80mm optimally reduces wave height discrepancies, although it corresponds with the highest recorded air suction volume of 576.81mm³. Alterations in baffle length have a marginal effect on reducing wave height differences. Meanwhile, modifying the baffle angle can decrease air suction volume, though its effectiveness varies in terms of wave height suppression.

2. The optimization of variables $L$, $H$, and $\theta$ was conducted using the --objective genetic algorithm NSGA-II, complemented by the multi-criteria decision making (MCDM) algorithm to pinpoint the optimal design parameters. The results revealed that the most effective suppression of liquid sloshing within the integrated tank is achieved with a baffle configuration of $L$ = 13 mm, $H$ = 49 mm, and $\theta$ = -20°. This optimization approach holds significant potential for enhancing the engineering design of integrated water tanks and offering innovative strategies for improving tank stability and performance. This method provides a novel and effective solution for the structural design of integrated water tanks, and has considerable value for practical applications.

## ACKNOWLEDGEMENTS

We acknowledge the support received from Yangzhou Industry Foresight and Common Key Technology Project (YZ20222028).

## CONFLICT OF INTEREST

The authors declare that they have no known competing financial interests or personal relationships that could have appeared to influence the work reported in this paper.

## AUTHORS CONTRIBUTION

**Fei Dong:** Conceptualization, Methodology, Formal Analysis, Investigation, Writing - original draft. **Xing Xu:** Investigation, Formal Analysis, Writing - original draft. **Wenyu Zhang:** Methodology, Writing - original draft, Formal Analysis, Data validation. **Wei Hu:** Writing - review & editing, Formal Analysis. **Xiaohui Cao:** Writing - review & editing, Formal Analysis.

## REFERENCES

Albadawi, A., Donoghue, D., Robinson, A., Murray, D., & Delauré, Y. (2013). Influence of surface tension implementation in volume of fluid and coupled volume of fluid with level set methods for bubble growth and detachment. *International Journal of Multiphase Flow*, *53*, 11-28. https://doi.org/10.1016/j.ijmultiphaseflow.2013.01.005

Baodong, S., Lifeng, W., Jianyun, L., & Heming, C. (2011). Multi‐objective optimization design of a micro‐channel heat sink using adaptive genetic algorithm. *International Journal of Numerical Methods for Heat & Fluid Flow*, *21*(3), 353-364. https://doi.org/10.1108/09615531111108512

Chen, B. F., & Nokes, R. (2005). Time-independent finite difference analysis of fully non-linear and viscous fluid sloshing in a rectangular tank. *Journal of Computational Physics*, *209*(1), 47-81. https://doi.org/10.1016/j.jcp.2005.03.006

Chu, C. R., Wu, Y. R., Wu, T. R., & Wang, C. Y. (2018). Slosh-induced hydrodynamic force in a water tank with multiple baffles. *Ocean Engineering*, *167*, 282-292. https://doi.org/10.1016/j.oceaneng.2018.08.049

Ebrahimian, M., Noorian, M. A., & Haddadpour, H. (2013). A successive boundary element model for investigation of sloshing frequencies in axisymmetric multi baffled containers. *Engineering Analysis with Boundary Elements*, *37*(2), 383-392. https://doi.org/10.1016/j.enganabound.2012.11.006

Faltinsen, O. M., & Timokha, A. N. (2010). A multimodal method for liquid sloshing in a two-dimensional circular tank. *Journal of Fluid Mechanics*, *665*, 457-479. https://doi.org/10.1017/S002211201000412X

Faltinsen, O., Rognebakke, O., & Timokha, A. (2005). Classification of three-dimensional nonlinear sloshing in a square-base tank with finite depth. *Journal of Fluids and structures*, *20*(1), 81-103. https://doi.org/10.1016/j.jfluidstructs.2004.08.001

Jin, X., Liu, M., Zhang, F., & Li, D. (2022). Mitigation of

liquid sloshing by multiple layers of dual horizontal baffles with equal/unequal baffle widths. *Ocean Engineering*, *263*, 112184. https://doi.org/10.1016/j.oceaneng.2022.112184

Kolaei, A., Rakheja, S., & Richard, M. J. (2015). A coupled multimodal and boundary-element method for analysis of anti-slosh effectiveness of partial baffles in a partly-filled container. *Computers & Fluids*, *107*, 43-58. https://doi.org/10.1016/j.compfluid.2014.10.013

Li, K., Chen, H., Xia, D., Zhang, H., Dou, B., Zhang, H., Liu, N., Su, L., Zhou, X., & Tu, R. (2023). Assessment method of the integrated thermal management system for electric vehicles with related experimental validation. *Energy Conversion and Management*, *276*, 116571. https://doi.org/10.1016/j.enconman.2022.116571

Liu, D., & Lin, P. (2008). A numerical study of three-dimensional liquid sloshing in tanks. *Journal of Computational physics*, *227*(8), 3921-3939. https://doi.org/10.1016/j.jcp.2007.12.006

Lu, L., Jiang, S. C., Zhao, M., & Tang, G. Q. (2015). Two-dimensional viscous numerical simulation of liquid sloshing in rectangular tank with/without baffles and comparison with potential flow solutions. *Ocean Engineering*, *108*, 662-677. https://doi.org/10.1016/j.oceaneng.2015.08.060

Ma, C., Xiong, C., & Ma, G. (2021). Numerical study on suppressing violent transient sloshing with single and double vertical baffles. *Ocean Engineering, 223*. https://doi.org/10.1016/j.oceaneng.2020.108557

Maleki, A., & Ziyaeifar, M. (2008). Sloshing damping in cylindrical liquid storage tanks with baffles. *Journal of Sound and Vibration*, *311*(1-2), 372-385. https://doi.org/10.1016/j.jsv.2007.09.031

Mitra, S., Upadhyay, P. P., & Sinhamahapatra, K. P. (2008). Slosh dynamics of inviscid fluids in two‐dimensional tanks of various geometry using finite element method. *International Journal for Numerical Methods in Fluids*, *56*(9), 1625-1651. https://doi.org/10.1002/fld.1561

Shao, J., Li, H., Liu, G., & Liu, M. (2012). An improved SPH method for modeling liquid sloshing dynamics. *Computers & Structures*, *100*, 18-26. https://doi.org/10.1016/j.compstruc.2012.02.005

Stern, F., Wilson, R., & Shao, J. (2006). Quantitative V&V of CFD simulations and certification of CFD codes. *International journal for numerical methods in fluids*, *50*(11), 1335-1355. https://doi.org/10.1002/fld.1090

Tian, Z., & Gu, B. (2019). Analyses of an integrated thermal management system for electric vehicles. *International Journal of Energy Research, 43*(11), 5788-5802. https://doi.org/10.1002/er.4679

Wu, G. X., Ma, Q. W., & Taylor, R. E. (1998). Numerical simulation of sloshing waves in a 3d tank based on a finite element method. *Applied Ocean Research, 20*(6), 337-355. https://doi.org/10.1016/S0141-1187(98)00030-3

Xue, M. A., Zheng, J., Lin, P., & Yuan, X. (2017). Experimental study on vertical baffles of different configurations in suppressing sloshing pressure. *Ocean Engineering*, *136*, 178-189. https://doi.org/10.1016/j.oceaneng.2017.03.031

Zhang, E. (2020). Numerical research on sloshing of free oil liquid surface based on different baffle shapes in rectangular fuel tank. *Proceedings of the Institution of Mechanical Engineers, Part D: Journal of Automobile Engineering*, *234*(2-3), 363-377. https://doi.org/10.1177/0954407019855569

Zhang, E., Zhu, W., & Wang, L. (2020). Influencing analysis of different baffle factors on oil liquid sloshing in automobile fuel tank. *Proceedings of the Institution of Mechanical Engineers, Part D: Journal of Automobile Engineering*, *234*(13), 3180-3193. https://doi.org/10.1177/0954407020919584

Zhang, Z., Wu, Q., Xie, Y., & Yu, H. (2023). Experimental and numerical investigations on the liquid tank sloshing in regular waves. *Ocean Engineering*, *271*, 113668. https://doi.org/10.1016/j.oceaneng.2023.113668